Materials Research. 2017; 20(6): 1445-1453
DOI: http://dx.doi.org/10.1590/1980-5373-MR-2017-0490
© 2017

Impact of Ni Substitution on Structural, Electrical and Thermoelectrical Properties of Zinc Alluminium Chromites Synthesized by sol-gel Route and their Photocatalytic Investigation

***Seema Pandurang Patil*[a], *Kallappa Ramchandra Sanadi*[b]*, *Vasant Baburao Helavi*[a]**

[a]*Department of chemistry, Rajaram college, Kolhapur, 416004, Maharashtra, India*
[b]*Department of chemistry, Doodhsakhar Mahavidyalaya, Bidri, Kolhapur, 416208, Maharashtra, India*

Received: May 13, 2017; Revised: June 27, 2017; Accepted: July 03, 2017

Nanostructured nickel substituted zinc alluminium chromites ($Zn_{1-x}Ni_xAlCrO_4$, where, x= 0.0, 0.25, 0.50, 0.75, 1.0) were prepared by simple, cost effective, sol-gel autocombustion method. Temperature of phase formation was analyzed by thermogravimetric and differential thermal analysis (TGA/DTA). Crystallographic studies of all the samples show formation of single cubic spinel phase only. The lattice parameter, crystallite size and X-ray density decreases with increase in Nickel content. The surface morphology of $Zn_{1-x}Ni_xAlCrO_4$ shows spherical interlinked morphology while elemental studies show desired composition. The nanosize of the synthesized material was confirmed by transmission electron microscopy (TEM) which was lies in between 19-25 nm. The DC conductivity as well as thermoelectric power studies of the samples reveals their semiconducting nature. The nanocrystalline chromite has optimal charge separation, which make them to enhance their photocatalytic efficiency. 0.100gm palladium loaded nickel alluminium chromite shows excellent mineralization in water.

Keywords: *Sol-gel chemistry, X-Ray Diffraction, TGA, Semiconductors, catalytic properties.*

1. Introduction

Now a day, metal oxide ceramic nano composite materials have become a focal point of scientific research because of their excellent performance, unique elemental comprehensive properties and potential applications in wide variety of fields[1-5]. The mixed metal oxides containing one or more transition metal ions are pioneer even in their bulk form for technological applications. It is due to their variable oxidation states and color ranges, which can be identified from their magnetic, optical and catalytic properties[6-7]. The magnetic properties of nanosized chromites are entirely different from those of their bulk counterparts, such as supermagnetic behavior, semiconducting nature and chemical photocatalytic properties. Nanosized chromites or ferrites with uniform particle size, surface area and narrow size distribution are desirable for applications in data storage devices, amplifiers, targeted drug delivery, ferrofluids, medical imaging and other biomedical applications, etc.[8-12].

Spinel type of nano chromites having general formula ACr_2O_4 (A = Ni, Zn, Fe, Co etc.) form an important class of metal oxides because of their explored applications in solid oxide fuel cells, magnetic devices, high electric resistive materials and significantly overlap of their optical absorption spectrum with UV radiation[13-16]. These properties are controlled by the nature of the participating ions, their charge and site dispersal amongst tetrahedral and octahedral sites. A literature survey indicates that considerable work has been done on zinc chromium ferrite, manganese chromium ferrite and nickel chromium ferrite[17-18]. The starting material of present chromite series, i.e., the compound $ZnAlCrO_4$ has been reported to be a normal spinel and the degree of inversion depends upon nature of substituted cations[19].

The constitutional and galvanic effects (charge separation) of chromites are found to be sensitive to their composition and microstructure, which are in turn dependent on their processing conditions and calcinating temperature[19]. In mixed metal chromites, the electric conductivity is characterized by their availability of electron, oxidation and reduction process between the divalent and trivalent chromium ions at octahedral sites. Thus, cation distributions along with their characteristic valency states within A and B sites play an important role in the conduction process.

In our previous studies[20,21], a sol-gel, self heated combustion method was developed to synthesize Cu-Cd and Co-Ni ferrites nanocrystalline powders. Spinel chromites prepared by sol-gel autocombustion route have wide spread applications in heterogeneous catalysis because of their high surface area, enhanced chemical activity, better stability and the reduced size. Heterogeneous photocatalyst were investigated for studying total oxidation of organic, inorganic water and air pollutants in last 20 years[22-26]. Textile dyes containing organic moieties and having low biodegradability have become major water environmental pollutant. These organic pollutants during dying lose their identity and get mixed with water streams in many industrial areas. So, to solve this eco-problem, photocatalytic degradation of these dyes using inorganic nano-semiconductor is a current need. Therefore, decomposition of organic dyes using various nanocomposites

*e-mail: sanadikishor@gmail.com

under irradiation of UV light is now emerging out as a new research area[27-29].

In the present work, we have attempted to investigate photocatalytic activity in nickel substituted zinc alluminium chromite. Moreover, we have doped nickel in zinc alluminium chromite due to its excellent physico-chemical properties. Pure nickel has ability to maximize reactive surface area of catalyst. It has also high power of resistance to corrosion, excellent ferromagnetic and electronic properties[30]. It is envisaged that such a compound drastically reduce the time for photo-mineralization of water. It is generally recognized that the final product depends upon some basic properties of powder, such as high purity, chemical homogeneity, particle size and its distribution. Thus, various preparation methods have been developed to obtain high quality powders, which may lead to improvement in efficiency of catalytic activity. The sol-gel method is preferred, as compared to other chemical routes for reducing the sintering time and temperature[31]. Moreover, sol-gel chemical process has advantage of inexpensive precursors, simple procedure for preparation and results in nanocrystalline homogeneous powders. In the present paper, we have reported the structural, electrical and photocatalytic properties of nickel substituted zinc alluminium chromite synthesized by sol-gel method.

2. Experimental Procedure

2.1 Sample preparation

Nanocrystalline chromite i.e. $Zn_{1-x}Ni_xAlCrO_4$ having compositions, x = 0.0, 0.25, 0.50, 0.75, 1.0 were synthesized by aqueous sol-gel auto-combustion method. The A.R. grade zinc nitrate [Zn $(No_3)_2.H_2O$], nickel nitrate [Ni $(No_3)_2.6H_2O$], alluminium nitrate [Al $(No_3)_3.9H_2O$], chromium nitrate [Cr $(No_3)_3.9H_2O$] and citric acid [$C_6H_8O_7.H_2O$] were used as starting materials. The fraction of metal nitrates and citric acid are used in ratio of 1:3 and then dissolved in water. A clear transparent solution was obtained after the reaction got completed. An appropriate amount of ammonia solution was then added to the solution to maintain the basic condition having pH value 9.5. During this process, the solution was continuously stirred using a magnetic stirrer. The mixed solution was evaporated on hot plate by stirring it at 363K for 1h. During evaporation, the solution became viscous and further heating led to brown jelly like appearance. Thereafter, all the remaining water was released from the solution and the mixture began to bubble and finally the gel automatically burnt with constant temperature having glowing froth. The reaction continued till the whole citrate complex was burnt. The auto-ignition was completed within few minutes yielding the brown colored ash like powder. The pelletized prepared chromite powders of all the samples were sintered separately at 963K for 8h . The outline of the procedure is as shown in schematic diagram 1.

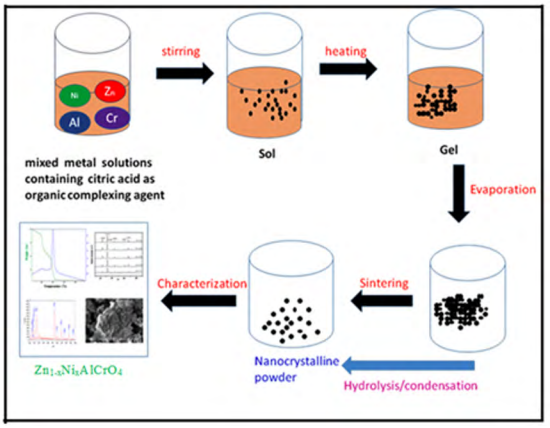

Scheme 1. Schematic presentation of sol-gel auto combustion method.

2.2 Characterization

To identify crystallization temperature and to ensure completion of reaction, the samples were characterized by thermogravimetric (TG) and differential thermal analysis (DTA). This was done using Nietzsche STA 409 TG-DTA instrument, at a heating rate of 283K/min in the nitrogen atmosphere. The crystallographic data of chromites were examined using X-ray diffractometer (PW-1830.Philips) with Cu Kα radiation (1.5405 Å). The X-ray powder diffractometer was operated at 60 kV and 40 mA and scanned within the 2θ range of 10-90°. The particle size of nanochromite was investigated by using a transition electron microscope (TEM). The morphology and chemical composition have been analyzed through scanning electron microscope (SEM) and energy dispersive X-ray analyzer (EDAX) respectively. Using 3-5mm thick disc samples, the dc electrical resistivity was measured as a function of temperature by the two probe method. A small constant current of 10 mA was passed through the sample to avoid the Joule heating. For electrical power measurement with temperature variation, sample was fitted directly in between Pt electrodes with a temperature gradient of 285.5K/cm across it. The temperature of both surfaces of the pellet was measured with the aid of thermocouples. The sign of the thermoelectrical voltage was taken as that of the cold surface. The thermoelectrical power of the sample α is calculated as $\alpha = \Delta V/\Delta T$. The opto-chemical properties were measured with the help of UV-Visible spectroscopy. Photocatalytic discernment of Rhodamine B (RhB) dye was carried out by using semi batch photocatalytic reactor with initial concentration of RhB 10mg/L. The quantitative determination of toxic organic was performed by measuring its absorbance in 200-800 nm with UV−Visible spectrophotometer. Photomineralisation of water (η) of RhB dye can be calculated by using formula as,

$$\eta = [Co - Ct]/Co \times 100 \qquad (1)$$

Where, Co and Ct is concentration of solution before and after irradiation of light at time t

2.3 Mechanism of heterogeneous catalysis

In heterogeneous catalysis, metal oxide nanoparticle shows the adsorption, desorption phenomenon. These processes of adsorption can activate the decisive chemical bonds of reactants. The desorption involve the removal of products from catalyst surface. Here, dye molecules are act as adsorbate and surface of chromite nanoparticle is a absorbent. The adsorption can be considered to involve the formation of bond between surface and gas phase or liquid phase molecule. This chemical bond is due to physical process hence they are weak. The dye molecule is sticking on catalyst surface, ability of sticking is governed by effectiveness of given molecule to dissipate its kinetic energy which nothing but electron pair excitation or photon excitation. The sticking molecule gets desorpted which give the mineralization of water with regain of catalyst. The reactivity mainly depends on the stoichiometric amount of reactant dispersed on surface. General reaction involved in catalysis as follows:

$$A + S \underset{}{\overset{k_{ads}}{\rightleftharpoons}} A \bullet S \; k_{des}$$

Where, S is a open surface site, A is active site, A • S is a surface bound molecule of A.

3. Results and Discussion

3.1 Thermal analysis

The synthesized nanocrystalline spinel phases of chromites were analyzed by thermo-analytical techniques. The TGA-DTA, traces for sample of $Zn_{1-x}Ni_xAlCrO_4$ (x = 0.0, 0.50, 1.0) are shown in Figure 1 (a-c). In Figure 1 (a) weight loss in TG curve is 62%. DTA traces shows presence of one exothermic peak. The peak around 484K in DTA curves was induced by decomposition of adsorbed water in inner and outer surface of crystal. Figure 1 (b and c) the DTA trace shows the presence of two exothermic peaks. The peak around 484K in DTA curves was induced by the decomposition of adsorbed water combined with citrate precursors in inner as well as outer surface of the crystals. The exothermic peak observed at 675K corresponds to the crystallization of spinel phase. The corresponding TG curves show four well defined weight loss from room temperature to 681K. A continuous loss of 5.72 wt% occurred in the first step, which indicates the decomposition of residual water from inner as well as outer surface of the material. The second weight loss showed the initiation of decomposition reaction triggered by citrate. The third weight loss indicates the decomposition of anhydrous metal complexes and fourth weight loss indicates the decomposition of citrates and nitrates from the material. 60 wt% losses occurred in-between second to fourth step. The overall analysis of TGA and DTA confirm the compound formation at 723K.

3.2 Crystallographic study

The typical X-ray diffraction patterns of the sample $Zn_{1-x}Ni_xAlCrO_4$ with x = 0.0, 0.25, 0.50, 0.75 and 1.0 are shown in Figure 2 (a). It confirms the formation of a single cubic spinel phase of the entire chromite samples[32-33]. The average crystallite size (D) was calculated using the Scherrer's formula[34]. The crystallite size of the samples were found to lie inbetween 18.4 to 29.1nm. The results are tabulated in Table 1.

The lattice parameter and X-ray density with their composition are also tabulated in Table 1. From this table, it is observed that lattice parameter, crystal size and X-ray density of all the samples decrease with increase in nickel content[35] and lattice parameter variation is shown in Figure 2 (b). This can be attributed to the difference in ionic radius of Ni^{2+} in comparison with Zn^{2+} as well as Cr^{2+} ions.

3.3.Elemental analysis

Figure 3 (a-c) shows the chemical framework for the $Zn_{1-x}Ni_xAlCrO_4$ (x = 0.0, 0.50,1.0) samples, which gives the elemental composition in the different samples. The samples clearly shows the presence of Zn, Ni, Al and Cr without any traces of impurities indicating purity of the sample and also no loss of prime metal contents. Thus, the result indicates that most of the undesired parent materials

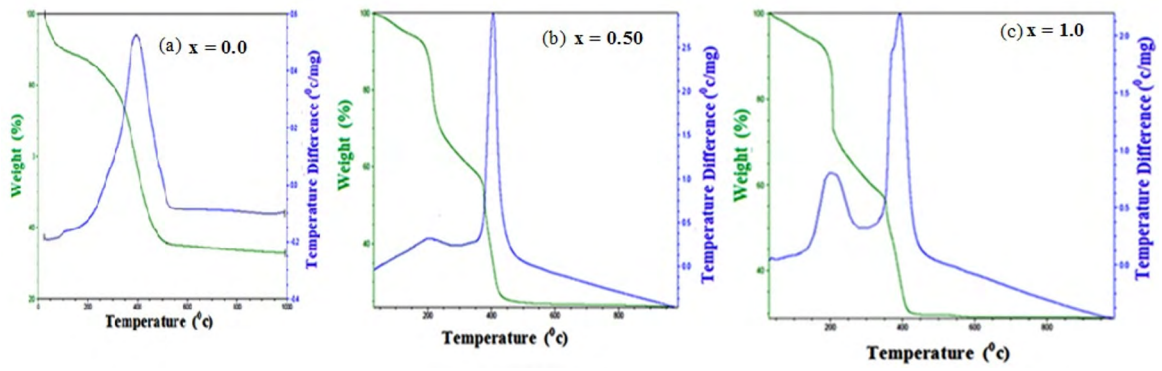

Figure 1. (a-c) TGA and DTA profiles of $Zn_{1-x}Ni_xAlCrO_4$ (where x = 0.0, 0.50, 1.0)

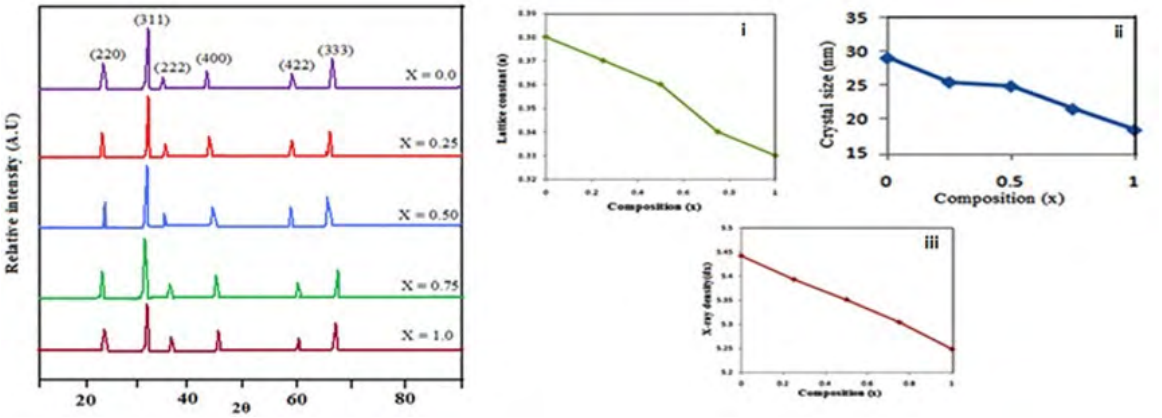

Figure 2. (a) XRD patterns of the system $Zn_{1-x}Ni_xAlCrO_4$ (where x = 0.0; 0.25; 0.50; 0.75; 1.0); (b)Variation of lattice constant (a), Crystal size (D) and X-ray density (dx)

Table 1. Lattice constant, Crystallite size, X-ray density, Grain size and Activation energy of the system $Zn_{1-x}Ni_xAlCrO_4$(x = 0.0, 0.25, 0.50, 0.75, 1.0)

Composition (X)	Lattice constant (A)	Crystallite size (nm)	X-ray density (dx)	Grain size from SEM (μm)	Activation Energy (ΔV) (eV)
X=0.0	8.38	9.1	5.442	0.451	0.564
X=0.25	8.37	25.5	5.393	-------	0.623
X=0.50	8.36	24.9	5.351	0.391	0.576
X=0.75	8.34	21.5	5.304	-------	0.591
X=1.0	8.33	18.4	5.248	0.340	0.587

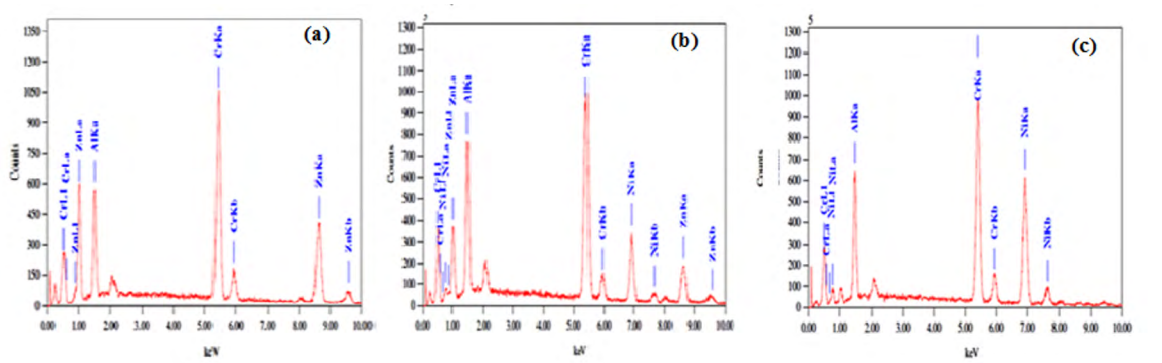

Figure 3. (a-c) EDS pattern for the sample $Zn_{1-x}Ni_xAlCrO_4$ (X = 0.0, 0.50, 1.0)

have been completely removed from the product. The results from EDAX spectra are shown in Table 2. From EDAX, it is observed that mass % of metals agrees well with theoretical metal mass % concentration.

3.4 Morphological investigation

The SEM analysis gives the morphology, micro structural information of materials. Typical scanning electron micrographs (SEM) of $Zn_{1-x}Ni_xAlCrO_4$ (where x = 0.0; 0.50; 1.0) images are shown in Figure 4 (a-c) after calcinations at 973K for 8 h. The grain size of the sample was calculated by using Cottrell's method[36,37]. The grain size lies in between 0.451 to 0.340 μm, which is included in Table 1. The larger grain size observed in SEM are due to the significant agglomeration of the crystallites. The SEM micrograph further reveals that though there are intergrannular pores but no prominent intragrannular pores are seen throughout the surface.

3.5 TEM analysis

TEM is a microscopic technique which was used to find out the outer morphology (shape of the nanoparticles) and mainly the particle size of the sample. The particle size distribution of typical compositions of $Zn_{1-x}Ni_xAlCrO_4$ (x = 0.0 and 1.0) obtained from TEM images are shown in Figure 5 (a-b). The image shows the co-existence of spherical

Table 2. Results of EDAX of $Zn_{1-x}Ni_xAlCrO_4$ (x = 0.0, 0.50, 1.0)

Composition	Zn atomic %		Ni atomic %		Al atomic %		Cr atomic %	
	Theo.	Obs.	Theo.	Obs.	Theo.	Obs.	Theo.	Obs.
0.0	34.98	34.81	-----	-----	29.19	29.08	34.99	34.72
0.50	20.50	20.47	16.22	16.09	28.89	28.71	33.99	33.84
1.0	-----	-----	35.24	35.15	29.29	29.09	34.89	34.71

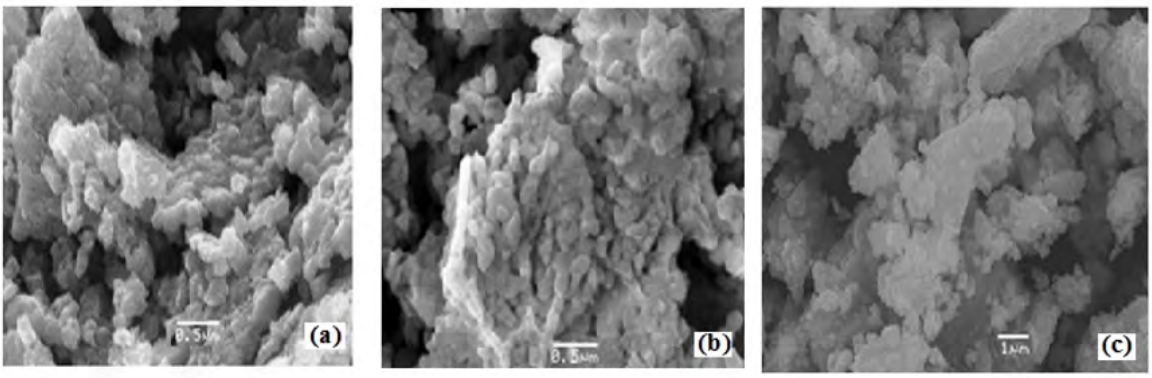

Figure 4. (a-c) SEM images of $Zn_{1-x}Ni_xAlCrO_4$ (x = 0.0; 0.50; 1.0)

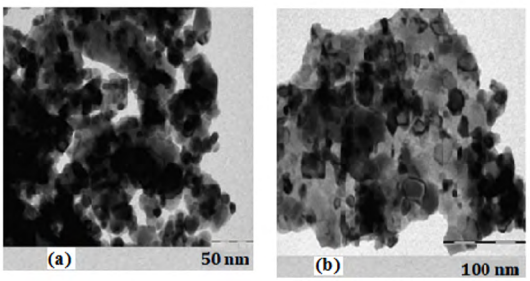

Figure 5. (a-b) TEM micrographs of $Zn_{1-x}Ni_xAlCrO_4$ (where x = 0.0; 1.0) respectively

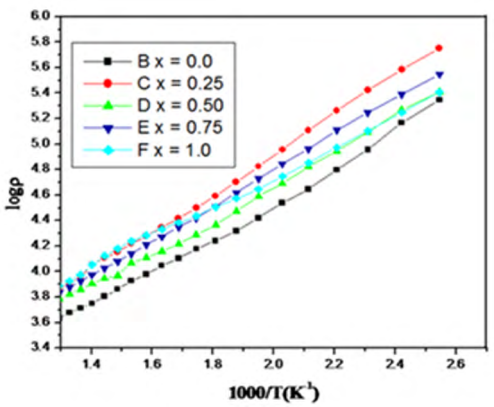

Figure 6. Variations in D.C. resistivity (log ρ) with temperature (1000/T) of $Zn_{1-x}Ni_xAlCrO_4$

particles with an average particle size of 25 nm, which was found to be in good agreement with those obtained from line broadening of x-ray diffraction analysis shown in Table 1. The similar is the case with other nanocrystalline materials[38].

3.6. Charge transfer phenomenon

The charge transfer phenomenon was investigated to interpret the results of photocatalytic action. The temperature dependant variations in electrical resistivity of $Zn_{1-x}Ni_xAlCrO_4$ (X = 0.0; 0.25; 0.50; 0.75; 1.0) is shown in Figure 6. From the Figure it is observed that the resistivity of all the analyzed samples decreases continuously with increasing temperature, signalizing semiconducting behavior of the chromites obeying Wilson's law[39]. A plot of logρ verses 10^3/T shows linear nature for all the compositions. The resistivity decreases with increase in temperature is due to the increase in deviation of mobility of the charge carriers. The electric conduction in chromites is assigned by the skipping of electrons in reduced reaction of chromium ions[40]. The formation of such chromium ion pairs assigned by the calcinating conditions and the amount of reduction of trivalent and divalent chromium ions at elevated temperature. The temperature dependence of galvanic conductivity in such a case involves less of temperature dependent concentration of carriers and is mostly related with temperature dependent mobility. The activation energies calculated from Wilson law are noted in Table 1. The decrease of activation energy in the ferromagnetic region is associated with effect of spin disordering. It is well know that the electron and hole hopping between the Cr^{+3}/ Cr^{+2}, Ni^{+3}/ Ni^{+2}, Zn^{+3}/ Zn^{+2} ions, is responsible for electrical conduction in mixed chromites.

The oxidation of Ni^{+2} to Ni^{+3} with increase in nickel content and reduction of Cr^{+3} to Cr^{+2} during sintering process

are favorable for photocatalytic reaction mechanism. This is also evinced from thermoelectric power studies. Moreover, the decrease in activation energy with increase in nickel content [Table 1] suggests increase in rate of photocatalytic reaction.

3.7. Thermoelectric power measurement

The compositional dependence of thermoelectric power measurement for the $Zn_{1-x}Ni_xAlCrO_4$ spinels with x = 0.0, 0.25, 0.5, 0.75 and 1.0 are shown in Figure 7. The graph ΔV against ΔT shows variation in thermal behavior. The sample having composition x=1.0 indicates p-type charge conveyors while all other samples reflecting n-type semiconductance. Similar is the results obtained by other researcher [41]. Nickel alluminium chromite is having positive slope, therefore gives holes as charge carriers, while all other samples (except x = 1.0) in this Figure are with negative slope indicating that in all the samples there are electrons as charge carriers. The most of charge carriers are electrons, which are generated from divalent chromium donor centers. So, the Cr rich samples show more n-type behavior as compared to Ni rich samples. Therefore all the samples show n-type semiconductivity except nickel alluminium chromite. This is ascribed to the hopping mechanism of polar electron and their abundant existence in almost all the compositions except x = 1[42].

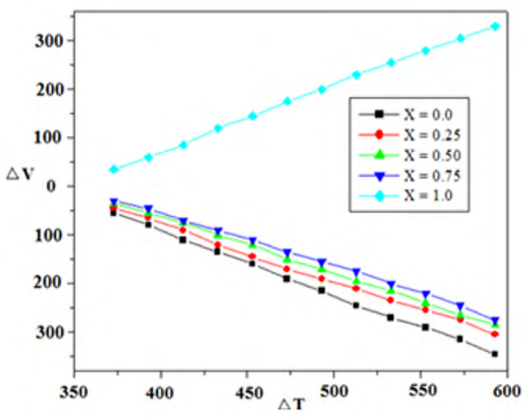

Figure 7. Plots of Δv Vs ΔT for the system $Zn_{1-x}Ni_xAlCrO_4$ ($0 \leq x \leq 1$)

A careful observation of thermoelectric generated voltage Vs temperature show a systematic decline in its slope with increase in nickel content and a dramatic jump from negative to positive value for the final x=1.0 composition. Thus it asserts the contribution from holes to photocatalytic activity with addition of nickel content.

3.8. Photocatalytic Performance

(a) Photocatalytic degradation of Rhodamine B by nickel substituted zinc alluminium chromites

The photodecomposition of Rhodamine B (RhB) with respect to irradiation time for the system $Zn_{1-x}Ni_xAlCrO_4$ is shown in the Figure 8 (a). From this Figure , it reveals that zinc alluminium chromite shows 64%, and nickel alluminium chromite shows 77% degradation of RhB within 240 min of irradiation time. The Photodegradation response of $Zn_{1-x}Ni_xAlCrO_4$ increases as nickel content increases and is more than zinc alluminium chromite. This is attributed to absorption band of nickel alluminium chromite semiconductor being wider than the band gap of zinc alluminium chromite. So, $NiAlCrO_4$ has been considered as an optimized catalyst for palladium loading for degradation of RhB Dye. In order to determine the optimal amount of catalyst dose, a series of experiments were carried out using different concentrations of Pd loading on $NiAlCrO_4$ catalyst varying from 0.020g to 0.100g at natural pH (7.86) with 10ppm RhB solution which was shown in Figure 8 (b). Maximum Mineralization 95 % has been observed at 0.100g and 85% at 0.020g in UV light after 25 min. The enhancement of the removal rate is due to the increase in the amount of catalyst weight, which increases the number of active sites available on the catalyst surface for the reaction.

(b) Photocatalytic degradation of Rhodamine B by Pd loading $NiAlCrO_4$.

Photocatalytic activity is mainly based on the semiconducting nature of heterogeneous catalyst having suitable energy band gap. Semiconductors can act as sensitizers for light induced redox processes due to their electronic structure, which is characterized by a filled valence band and an empty conduction band[43]. The decrease in activation energy with increase in nickel content Table.1 reduces the absorption of UV radiation, again justifying the addition of Ni to $ZnAlCrO_4$. Further reduction in absorption of UV radiation is obtained by addition of Palladium and is quite obvious. The novelty lies in decrease of absorption with increase in Ni content. UV irradiation of these semiconducting material resulted in generation of conduction band electron and valence band hole, which is shown in scheme 2. The holes are extremely oxidized to react with water present in dye to form hydroxyl radicals. The electron in conduction band reduces the oxygen to give hydroxyl radical.[44-48] The species formed from electron and hole having strong oxidizing power, it further leads to oxidizing organic compound to CO_2 and H_2O[49,50]. From earlier reports, photocatalytic reaction mechanism of degradation of dye is as given bellow [51]:

Oxidative reactions due to photocatalytic effect:

$$UV + Chromite \longrightarrow (h_{vb}^{+} + e_{eb}^{-}) \quad (2)$$

$$Chromite\,(h_{vb}^{+}) + H_2O \longrightarrow H^{+} + OH^{\cdot} \quad (3)$$

$$2h^{+} + 2H_2O \longrightarrow 2H^{+} + H_2O_2 \quad (4)$$

$$H_2O_2 \longrightarrow HO^{\cdot} + OH^{\cdot} \quad (5)$$

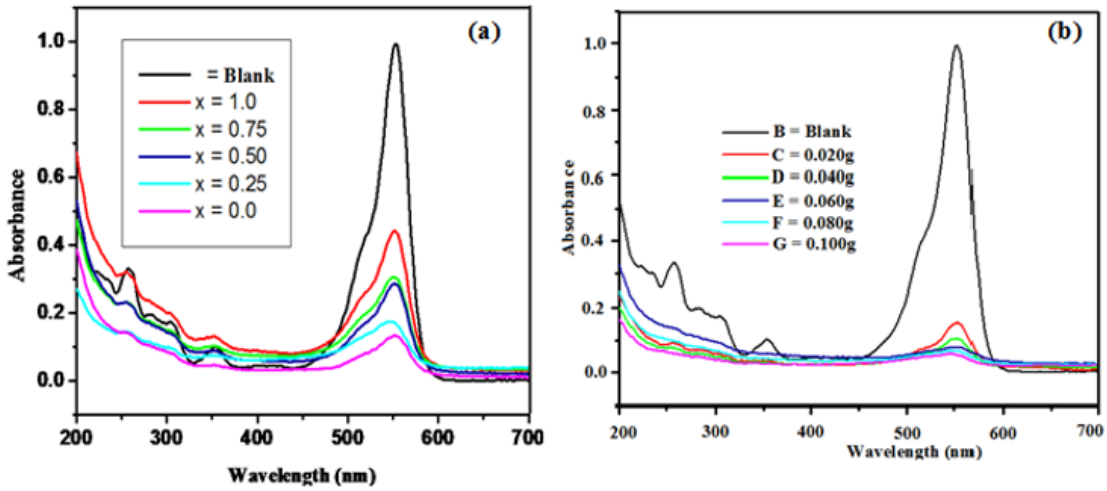

Figure 8. (a) Photocatalytic degradation of Rhodamine B by $Zn_{1-x}Ni_xAlCrO_4$ ($0 \leq x \leq 1$); (b) Photocatalytic degradation of Rhodamine B by Pd loaded NiAl chromites.

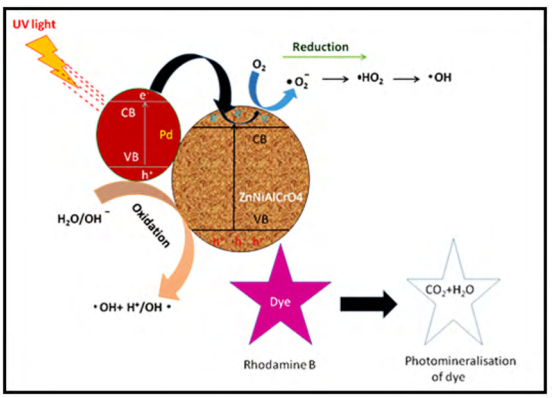

Scheme 2. Photocatalytic degradation mechanism of Dye.

$$\text{Net reaction: Chromite } (h_{vb}^{+}) + OH^{-} \longrightarrow OH^{\cdot} \quad (6)$$

The reductive reaction due to photocatalytic effect:

$$\text{Chromite } (e_{cb}^{-}) + O_2 \longrightarrow O_2^{\cdot} \quad (7)$$

$$O_2^{\cdot -} + HO^{\cdot}{}_2 + H^{+} \longrightarrow H_2O_2 + O2 \quad (8)$$

$$HOOH \longrightarrow HO^{\cdot} + OH^{\cdot} \quad (9)$$

$$\text{Net reaction: } - \text{Chromite } (e_{cb}^{-}) + O_2 + H^{+} \longrightarrow OH \quad (10)$$

$$\text{Overall reaction: } - \text{Dye} + 2OH^{\cdot} \longrightarrow \text{Degradation of Dye} \quad (11)$$

4. Conclusions

Nanosized nickel substituted zinc alluminium chromite powders were successfully synthesized by the sol-gel auto-combustion method using citric acid as combustion agent. The temperature for formation of the crystallization phase has been confirmed by TGA/DTA data. XRD data reveals the formation of cubic single spinel phase only. The lattice parameter decreases with increase in nickel content. The TEM studies show average particle size of 25 nm. The stoichiometry of these samples is in close agreement to the calculated data. The study of DC electrical resistivity shows its semiconducting nature. It is observed that the activation energy decreases with increase in the nickel contents. The thermoelectrical power measurements shows that only nickel alluminium chromite is p-type and all other samples are n-type semiconductor. The redox reaction is mandatory for effective photocatalytic activity, which is verified by the charge transport phenomena. Decrease in activation energy with increase in nickel content also justifies the very purpose of nickel substitution for increasing the rate of photocatalytic reaction. The nickel alluminium chromite loaded with palladium was observed to have excellent photo mineralization of water on reduced time scale.

5. Acknowledgements

One of the author (SPP) thankfully acknowledgement to Department of chemistry, Shivaji university Kolhapur for valuable guidance and suggestion.

Conflict of interest: the authors declare that there is no conflict of interest in publishing this funded work. Further, none of them have received any grant to support this work.

6. References

1. Karmhag R, Tesfamichael T, Wäckelgård E, Niklasson A, Nygren M. Oxidation Kinetics of Nickel Particles: Comparison Between Free Particles and Particles in an Oxide Matrix. *Solar Energy*. 2000;68(4):329-333.

2. Hyeon T. Chemical synthesis of magnetic nanoparticles. *Chemical Communications*. 2003;(8):927-934.

3. Yan E, Xu E, Wang E, Wang C, Yang C, Xie Y, et al. Preparation and Research on the Performance of PPV/PVP/Au Composite Nanofibers by Electrospinning. *International Journal of Eletrochemical Science*. 2013;8:12683-12691.

4. Lee IS, Lee N, Park J, Kim BH, Yi YW, Kim T, et al. Ni/NiO Core/Shell Nanoparticles for Selective Binding and Magnetic Separation of Histidine-Tagged Proteins. *Journal of the American Chemical Society*. 2006;128(33):10658-10659.

5. Tseng WJ, Chen CM. Dispersion and rheology of nickel nanoparticle inks. *Journal of Materials Science*. 2006;41(4):1213-1219.

6. Izyumkaya N, Alivov Y, Morkoc H. Oxides, Oxides, and More Oxides: High-κ Oxides, Ferroelectrics, Ferromagnetics, and Multiferroics. *Critical Reviews in Solid State and Materials Sciences*. 2009;34(3-4):89-179.

7. Modeshia DR, Walton RI. Solvothermal synthesis of perovskites and pyrochlores: crystallisation of functional oxides under mild conditions. *Chemical Society Reviews*. 2010;39(11):4303-4325.

8. Shinkai M. Functional magnetic particles for medical application. *Journal of Bioscience and Bioengineering*. 2002;94(6):606-613.

9. Lübbe AS, Alexiou C, Bergemann C. Clinical Applications of Magnetic Drug Targeting. *Journal of Surgical Research*. 2000;95(2):200-2006.

10. Tiefenauer LX, Tschirky A, Kühne G, Andres RY. In vivo evaluation of magnetite nanoparticles for use as a tumor contrast agent in MRI. *Magnetic Resonance Imaging*. 1996;14(4):391-402.

11. Skmoski R. Nanomagnetics. *Journal of Physics: Condensed Matter.* 2003;15(20):R841.

12. Fischer P, Kim DH, Chao W, Liddle JA, Anderson EH, Attwood DT. Soft X-ray microscopy of nanomagnetism. *Materials Today*. 2006;9(1-2):26-33.

13. Henderson MA, Engelhard MH. Impact of a Mixed Oxide's Surface Composition and Structure on Its Adsorptive Properties: Case of the (Fe,Cr)3O4(111) Termination of the a-(Fe,Cr)2O3(0001) Surface. *The Journal of Physical Chemistry C*. 2014;118(50):29058-29067.

14. Kitano M, Hara M. Heterogeneous photocatalytic cleavage of water. *Journal of Materials Chemistry*. 2010;20(4):627-641.

15. Wang C, Liu H, Sun ZM. Heterogeneous Photo-Fenton Reaction Catalyzed by Nanosized Iron Oxides for Water Treatment. *International Journal of Photoenergy*. 2012;2012:801694. DOI: 10.1155/2012/801694

16. Deshpande K, Mukasyan A, Verma A. Aqueous Combustion Synthesis of Strontium-Doped Lanthanum Chromite Ceramics. *Journal of the American Ceramic Society*. 2003;86(7):1149-1154.

17. Khan MN, Ahmed A, Darshane VS. X-ray, electrical conductivity and infrared studies of the system Zn1-x CO x Mn1-x Fe x CrO4. *Journal of Materials Science*. 1998;24(1):163-166.

18. Baltzer PK, Wejtwicz PJ, Robbins MB, Lopatin E. Exchange Interactions in Ferromagnetic Chromium Chalcogenide Spinels. *Physical Review*. 2006;151(2):367.

19. Gharagozlou M. Influence of calcination temperature on structural and magnetic properties of nanocomposites formed by Co-ferrite dispersed in sol-gel silica matrix using tetrakis(2-hydroxyethyl) orthosilicate as precursor. *Chemistry Central Journal*. 2011;5:19.

20. Hankare PP, Sanadi KR, Pandav RS, Patil NM, Garadkar KM, Mulla IS. Structural, electrical and magnetic properties of cadmium substituted copper ferrite by sol-gel method. *Journal of Alloys and Compounds*. 2012;540:290-296.

21. Hankare PP, Sanadi KR, Garadkar KM, Patil NM, Mulla IS. Synthesis and characterization of nickel substituted cobalt ferrite nanoparticles by sol-gel auto-combustion method. *Journal of Alloys and Compounds*. 2013;553:383-388.

22. Schiavello M, ed. *Heterogeneous Photocatalysis*. Hoboken: Wiley; 1997. 208 p.

23. Bahnemann D. Photocatalytic Detoxification of Polluted Waters. In: Boule P, ed. *Handbook of Environmental Photochemistry*. Berlin: Springer; 1999. p. 285-351.

24. Bahnemann D, Cunningham J, Fox MA, Pelizzetti E, Pichat P, Serpone N. Photocatalytic Treatment of Waters. In: Helz GR, Zepp RG, Crosby DG, eds. *Aquatic and Surface Photochemistry*. Boca Raton: CRC Press; 1993.

25. Ertl G, Knozinger H, Weitkamp J, eds. *Handbook of Heterogeneous Catalysis*. Weiheim: VCH-Wiley;1997.

26. Ollis DF, Al-Ekabi H, eds. *Photocatalytic Purification and Treatment of Water and Air*. Amsterdam: Elsevier; 1993.

27. Liu X, Chen K, Shim JJ, Huang J. Facile synthesis of porous Fe2O3 nanorods and their photocatalytic properties. *Journal of Saudi Chemical Society*. 2015;19(5):479-484.

28. Karimi L, Zohoori S, Yazdanshenas ME. Photocatalytic degradation of azo dyes in aqueous solutions under UV irradiation using nano-strontium titanate as the nanophotocatalyst. *Journal of Saudi Chemical Society*. 2014;18(5):581-588.

29. Xu SH, Shangguan WH, Yuan J, Shi JW, Chen MX. Photocatalytic properties of bismuth titanate Bi12TiO20 prepared by co-precipitation processing. *Materials Science and Engineering: B*. 2007;137(1-3):108-111.

30. Nickel. In: Anthony JW, Bideaux RA, Bladh KW, Nichols MC, eds. *Handbook of Mineralogy*. Chantilly: Mineralogical Society of America. Available from: <http://www.handbookofmineralogy.org/pdfs/nickel.pdf>. Access in: 15/7/2017.

31. Sinha A, Nayar S, Murthy GVS, Joy PA, Rao V, Ramachandrarao P. Biomimetic synthesis of superparamagnetic iron oxide particles in proteins. *Journal of Materials Research*. 2003;18(6):1309-1313.

32. Gene SA, Saion E, Shaari AH, Kamarudin MA, Al-Hada NM, Kharazmi A. Structural, Optical, and Magnetic Characterization of Spinel Zinc Chromite Nanocrystallines Synthesised by

Thermal Treatment Method. *Journal of Nanomaterials*. 2014;2014:416765. DOI: 10.1155/2014/416765.

33. Edrissi M, Keshavarz AR. Synthesis of Cobalt Chromite Nanoparticles by Thermolysis of Mixed Cr3+ and Co2+ Chelates of 2- Mercaptopyridin N-Oxide. *Nano-Micro Letters*. 2012;4(2):83-89.

34. Cullity BD. *Elements of X-ray Diffraction*. Reading: Addison-Wesley; 1978.

35. Arulmurugan R, Jeyadevan B, Vaidyanathan G, Sendhilnathan S. Effect of zinc substitution on Co-Zn and Mn-Zn ferrite nanoparticles prepared by co-precipitation. *Journal of Magnetism and Magnetic Materials*. 2005;288:470-477.

36. Wells OC. *Scanning Electron Microscopy*. New York: McGraw Hill; 1974.

37. Gopalan EV, Malini KA, Sagar S, Sakthi Kumar D, Yoshida Y, Al-Omari IA, et al. Mechanism of ac conduction in nanostructured manganese zinc mixed ferrites. *Journal of Physics D: Applied Physics*. 2009;42(16):165005.

38. Sattar AA. Temperature Dependence of the Electrical Resistivity and Thermoelectric Power of Rare Earth Substituted Cu-Cd ferrite. *Egyptian Journal of Solids*. 2003;6(2):113-122.

39. Klinger MI. Two-phase polaron model of conduction in magnetite-like solids. *Journal of Physics C: Solid State Physics*. 1975;8(21):3595.

40. Brahma S, Choudhary RNP, Shivashankar SA. Structural, thermal and electrical characterization of NdLiMo2O8 electroceramics, using impedance spectroscopy. *Journal of Physics and Chemistry of Solids*. 2012;73(2):357-362.

41. Berkowitz AE, Scuele WJ, Flanders PJ. Influence of Crystallite Size on the Magnetic Properties of Acicular γ-Fe2O3 Particles. *Journal of Applied Physics*. 1968;39(2):1261.

42. Nathani H, Gubbala S, Misra RDK. Magnetic behavior of nanocrystalline nickel ferrite: Part I. The effect of surface roughness. *Materials Science and Engineering: B*. 2005;121(1-2):126-136.

43. Lewis LN. Chemical catalysis by colloids and clusters. *Chemical Reviews*. 1993;93(8):2693- 2730.

44. Gómez E, Gónzalez B, Domínguez A, Tojo E, Tojo J. Dynamic Viscosities of a Series of 1-Alkyl-3-methylimidazolium Chloride Ionic Liquids and Their Binary Mixtures with Water at Several Temperatures. *Journal of Chemical & Engineering Data*. 2006;51(2):696-701.

45. Andreozzi R, Caprio V, Insola A, Marotta R. Advanced oxidation processes (AOP) for water purification and recovery. *Catalysis Today*. 1999;53(1):51-59.

46. Kümmerer K. Resistance in the environment. *The Journal of Antimicrobial Chemotheraphy*. 2004;54(2):311-320.

47. Rauf MA, Salman Ashraf S. Fundamental principles and application of heterogeneous photocatalytic degradation of dyes in solution. *Chemical Engineering Journal*. 2009;151(1-3):10-18.

48. Valenzuela MA, Bosch P, Jimenez-Becerrill J, Quiroz O, Paez AI. Preparation, characterization and photocatalytic activity of ZnO, Fe2O3 and ZnFe2O4. *Journal of Photochemistry and Photobiology A: Chemistry*. 2002;148(1-3):177-182.

49. Zhang L, Zhou X, Guo X, Song X, Liu X. Investigation on the degradation of acid fuchsin induced oxidation by MgFe2O4 under microwave irradiation. *Journal of Molecular Catalysis A: Chemical*. 2011;335(1-2):31-37.

50. Zhang H, Chen G, Bahnemann DW. Photoelectrocatalytic materials for environmental applications. *Journal of Materials Chemistry*. 2009;19(29):5089-5121.

51. Daneshvar N, Salari D, Khataee AR. Photocatalytic degradation of azo dye acid red 14 in water on ZnO as an alternative catalyst to TiO2. *Journal of Photochemistry and Photobiology A: Chemistry*. 2004;162(2-3):317-322.